Nano Energy 70 (2020) 104473

Contents lists available at ScienceDirect

Nano Energy

journal homepage: http://www.elsevier.com/locate/nanoen

Full paper

Study of vibrational droplet triboelectric nanogenerator on structural and operational parameters

Jing Ding [a], Wen-Quan Tao [a,*], Shih-Kang Fan [b,**]

[a] Key Laboratory of Thermo-Fluid Science and Engineering of MOE, Xi'an Jiaotong University, Xi'an, 710049, China
[b] Department of Mechanical and Nuclear Engineering, Kansas State University, Manhattan, KS, 66506, USA

ARTICLE INFO

Keywords:
Triboelectric nanogenerator
Water droplet
Device structure
Optimal load resistance
Serial-droplet

ABSTRACT

Structural parameter, such as device structure, and operational parameters, such as load resistance and droplet arrangement, were studied on the vibrational droplet triboelectric nanogenerators. Single-droplet devices with different structures were tested and theoretically analyzed. It is discovered that the device structure influences the output power by changing the triboelectric charge and the tribo/inductive capacitance ratio. The dependence of the optimal load resistance on the droplet number and the vibration frequency was experimentally studied with parallel-droplet devices. Calculations were performed to quantify the relationship between the optimal load resistance and the influential factors. The output performance of the serial-droplet device was measured and compared with that of the single-droplet and parallel-droplet devices. It is found that their output performance is significantly affected by the parasitic capacitance.

1. Introduction

Triboelectric nanogenerator (TENG) is a novel energy harvesting technology that converts the mechanical energy into electricity by utilizing triboelectricity [1–3]. A large variety of the TENGs have been developed with different structural designs [4–15] for the applicability and flexibility for various energy sources [15–26] and various applications [2,27–37]. The vibrational droplet triboelectric nanogenerator converts the vibrational energy into electrical energy on the basis of the contact electrification between the liquid droplet and the solid materials. Such devices emerge as an alternative to the TENGs based on the triboelectric effect of two different solid materials. The presence of the liquid droplet eliminates the abrasion between solid materials, which helps to avoid material degradation and performance decrement and improves the stability and durability [38–43]. In order to improve the output performance of the vibrational droplet TENGs, extensive study has been conducted on the structural and operational parameters, such as droplet volume, ion concentration, vibration frequency, vibrational amplitude, load resistance, bias voltage, and temperature [44–48]. However, there still exist several important issues that have not been clearly elucidated, such as the device structure, the optimal load resistance, and the serial-droplet device.

Various device structures have been reported in the literature. The device proposed by Krupenkin and Taylor [44] consisted of a hydrophobic top plate containing a dielectric layer and a hydrophilic bottom plate without a dielectric layer. The device developed by Kwon et al. [45] was composed of hydrophobic top and bottom plates both without a dielectric layer. A more common structure, which includes a hydrophobic top plate and a hydrophilic bottom plate both without a dielectric layer, was adopted in some vibrational droplet TENGs [46–48]. Until now, the output performance of different device structures has not been compared and the optimal structure for better output performance has not been pointed out. Therefore, the first focus of this paper is the effects of the device structures.

It has been reported that the output power of the vibrational droplet TENG first increased and then decreased as the load resistance increased [47,48], which is also found in other TENGs [49–51]. There exists an optimal load resistance at which the output power reaches the maximum value, which is crucial for the performance optimization. However, how the optimal load resistance is influenced is still not clearly understood. Hence, the second focus of this paper is the dependence of the optimal load resistance.

For the practical application of powering electronic devices, parallel droplets were formed to increase the output power [46]. In addition to

* Corresponding author.
** Corresponding author.
E-mail addresses: dingjing.09@stu.xjtu.edu.cn (J. Ding), wqtao@mail.xjtu.edu.cn (W.-Q. Tao), skfan@ksu.edu (S.-K. Fan).

https://doi.org/10.1016/j.nanoen.2020.104473
Received 9 November 2019; Received in revised form 21 December 2019; Accepted 6 January 2020
Available online 24 January 2020

the parallel-droplet device, the serial-droplet device that contains droplets connected in series is also an alternative. However, the output performance of the serial-droplet device is rarely reported. Thus, the third focus of this paper is the serial-droplet device.

In this paper, the output performance of the vibrational droplet TENGs with different structures were measured. The influencing mechanism of the device structure on the output power was further investigated by theoretical analysis. Next, the dependence of the optimal load resistance on the droplet number and the vibration frequency was experimentally studied. Empirical fitting and theoretical calculations were also performed to clarify the quantitative relationship between the optimal load resistance and the related factors. Furthermore, the output performance of the serial-droplet device was measured and compared with that of the single-droplet and parallel-droplet devices.

2. Methods

2.1. Device setup

Generally, the vibrational droplet TENG is composed of a top plate, a water droplet, and a bottom plate. For the study of device structures, single-droplet devices with different top plates and bottom plates were used, as shown in Fig. 1. ITO glass, SU-8, and Teflon were employed as the electrode, dielectric layer, and hydrophobic layer, respectively. For the study of optimal load resistance, the parallel-droplet devices were used, as shown in Fig. 2a. An ITO glass coated with a hydrophobic layer Shieldex served as the hydrophobic top plate, while an ITO glass was used as a hydrophilic bottom plate. In order to fix the locations of the droplets and prevent them from merging with one another, a patterned hydrophobic layer Shieldex was fabricated on the bottom plate. In the study of serial-droplet device, both the top and bottom plates were composed of a patterned ITO electrode and a patterned hydrophobic layer Shieldex for the serial connection of the water droplets, as shown in Fig. 2b.

2.2. Device fabrication

For the single-droplet devices, the fabrication process is described as follows. ITO glass was immersed in acetone, isopropanol, and deionized water in sequence and sonicated in the ultrasonicator for at least 5 min. Then, the ITO glass was dried by CDA (clean dry air) and baked at 150 °C for 5 min. SU-8 2002 (Microchem) was spin-coated on the ITO glass at 4500 rpm for 60 s as a dielectric layer and soft baked at 95 °C for 5 min. After exposed to UV light with a dose of 200 mJ cm^{-2}, the glass was soft baked at 95 °C for 5 min and then hard baked at 150 °C for 30 min. 0.5% Teflon AF1600 (DuPont) was spin-coated on the ITO glass at 3000 rpm for 30 s as a hydrophobic layer and hard baked at 150 °C for 30 min. The thickness of SU-8 and Teflon were measured to be 2.6 μm and 70 nm, respectively. The dielectric layer and the hydrophobic layer are not always required, depending on the structure of the device.

For the parallel-droplet devices, the fabrication process is similar to that of the single-droplet devices, except that Shieldex supplied by Integrated Surface Technologies was used as the hydrophobic layer instead of Teflon. Shieldex was deposited on the ITO glass in the chemical vapor deposition system (Integrated Surface Technologies BL200) for 15 min with the electrode power of 105 W and the chamber pressure of 200 mTorr. The thickness of Shieldex was 37 nm. The bottom plate with a patterned hydrophobic layer was fabricated by photolithography, deposition, and lift-off processes, which is described as follows. Photoresist AZ5214 (Clariant) was spin-coated on the ITO glass at 4000 rpm for 40 s and soft baked at 110 °C for 90 s. Then, the glass was covered by a mask and exposed to UV light with a dose of 140 mJ cm^{-2}. Subsequently, the glass was immersed in developer NMD-3, rinsed by deionized water, dried by CDA and baked at 145 °C for 5 min, achieving patterned photoresist. After Shieldex was deposited on the ITO glass with patterned photoresist, the Shieldex was patterned with a lift-off process by immersing the glass in the stripper NMP, resulting in a patterned hydrophobic layer.

For the serial-droplet device, both the ITO electrode and the hydrophobic layer were patterned. The patterned ITO electrodes were fabricated by photolithography and wet etching in aqua regia (HNO_3:HCl:H_2O = 1:3:6) at 49 °C. Then, the patterned hydrophobic layer was fabricated by photolithography, deposition, and lift-off, as described in the fabrication of the parallel-droplet devices.

2.3. Performance test system

The performance test system of the vibrational droplet TENG is shown in Fig. S1. The bottom plate of the TENG was fixed on the electromagnetic shaker (Labworks ET-126-4), while the top plate was attached to the cantilever of the elevator. The gap between the top and the bottom plates was modulated through the elevator. The bottom plate was oscillated by the electromagnetic shaker powered by the electrical signal generated by the function generator (Agilent 33210A) and amplified by the power amplifier (Labworks PA-141). The electrical signal produced by the TENG was measured by the electrometer

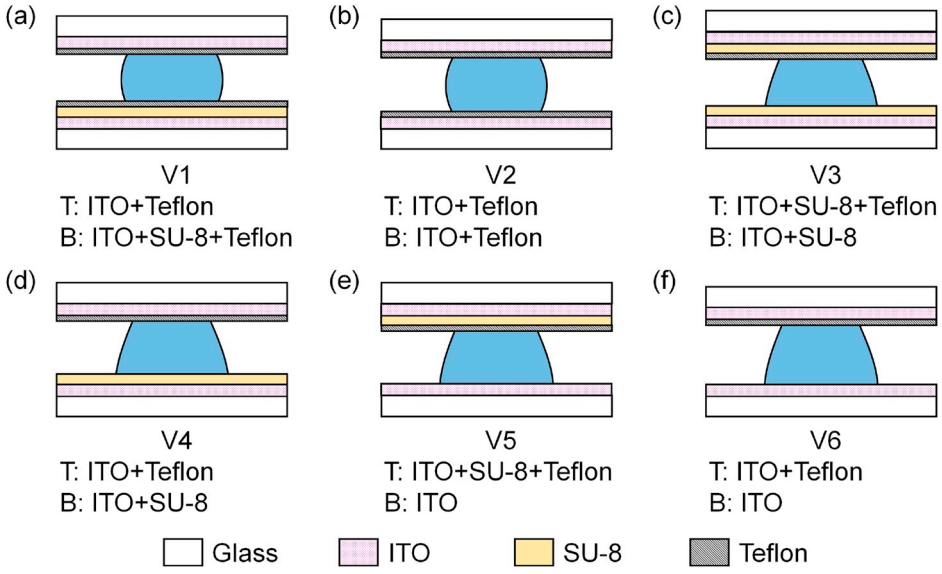

Fig. 1. Schematic of different device structures. (a) Structure V1 used ITO+Teflon as the top plate and ITO+SU-8+Teflon as the bottom plate. (b) Structure V2 used ITO+Teflon as the top plate and ITO+Teflon as the bottom plate. (c) Structure V3 used ITO+SU-8+Teflon as the top plate and ITO+SU-8 as the bottom plate. (d) Structure V4 used ITO+Teflon as the top plate and ITO+SU-8 as the bottom plate. (e) Structure V5 used ITO+SU-8+Teflon as the top plate and ITO as the bottom plate. (f) Structure V6 used ITO+Teflon as the top plate and ITO as the bottom plate.

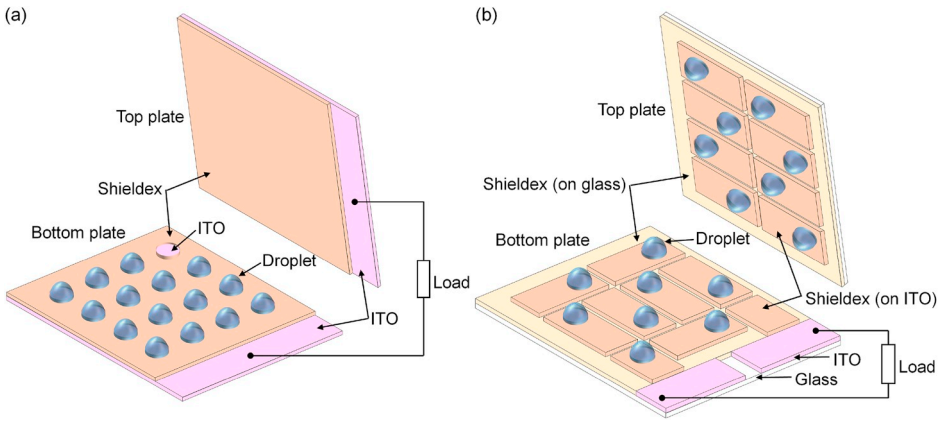

Fig. 2. Schematic of the parallel-droplet and serial-droplet devices. (a) Parallel-droplet device. (b) Serial-droplet device.

(Keithley 6517B) and collected by the LabVIEW program.

3. Theoretical model

Moon et al. [46] proposed a theoretical model to elucidate the working principle of the vibrational droplet TENG which contained a hydrophobic top plate and a hydrophilic bottom plate. The model was adopted and extended here to describe the working process of other device structures, as shown in Fig. 3. When the water droplet is in contact with the solid, an electrical double layer (EDL) is formed at the liquid-solid interface [52–55], resulting in a negatively charged hydrophobic layer and a positively charged water droplet. Since the structure of the EDL is similar to that of a capacitor, it can be treated as a capacitor [56–58]. When the bottom plate is vertically vibrated, the gap between the top and bottom plates is varied, resulting in variations of the contact areas of the droplet with the top plate A_T and the bottom plate A_B. Given that the capacitances of the top and bottom EDL ($C_T(t)$, $C_B(t)$) are proportional to the contact areas ($A_T(t)$, $A_B(t)$), the capacitances can be presented by

$$C_T(t) = \frac{\varepsilon_0 A_T(t)}{\frac{t_H}{\varepsilon_H} + \frac{t_D}{\varepsilon_D} + \frac{t_L}{\varepsilon_L}} \tag{1}$$

$$C_B(t) = \frac{\varepsilon_0 A_B(t)}{\frac{t_H}{\varepsilon_H} + \frac{t_D}{\varepsilon_D} + \frac{t_L}{\varepsilon_L}} \tag{2}$$

where t_H, t_D, and t_L (ε_H, ε_D, and ε_L) are the thickness (relative permittivities) of the hydrophobic layer, dielectric layer, and EDL, respectively, and ε_0 is permittivity of vacuum.

Before the vibration commences, the top capacitor C_T and the bottom capacitor C_B are in equilibrium that V_T=V_B, as shown in Fig. 3a. The corresponding equivalent electrical circuit is depicted in Fig. 3c, where Q_T and Q_B are the surface charges stored on the capacitors C_T and C_B, respectively. Hence, $Q_T = C_T V_T$ and $Q_B = C_B V_B$. When the droplet is squeezed or drawn due to the vertical oscillation of the bottom plate, the contact areas A_T and A_B and thus the capacitors C_T and C_B change, leading to variations in V_T and V_B. As a result, a voltage difference V_B-V_T is established, driving the electrons flow from one plate to the other plate. Consequently, electrical current is generated in the external circuit, as shown in Fig. 3b. The corresponding equivalent electrical circuit is depicted in Fig. 3d. Assuming that the bottom plate starts to approach the top plate at $t = 0$, the governing equation of the electrical circuit shown in Fig. 3d can be expressed as

$$(R_{load} + R_L)\frac{dq(t)}{dt} = V_B(t) - V_T(t) = \frac{Q_B - q(t)}{C_B(t)} - \frac{Q_T + q(t)}{C_T(t)} \tag{3}$$
$$t = 0, \quad q = 0$$

where R_{load} is the load resistance, R_L is the droplet resistance, and $q(t)$ is the increment (decrement) of the top (bottom) charge at time t.

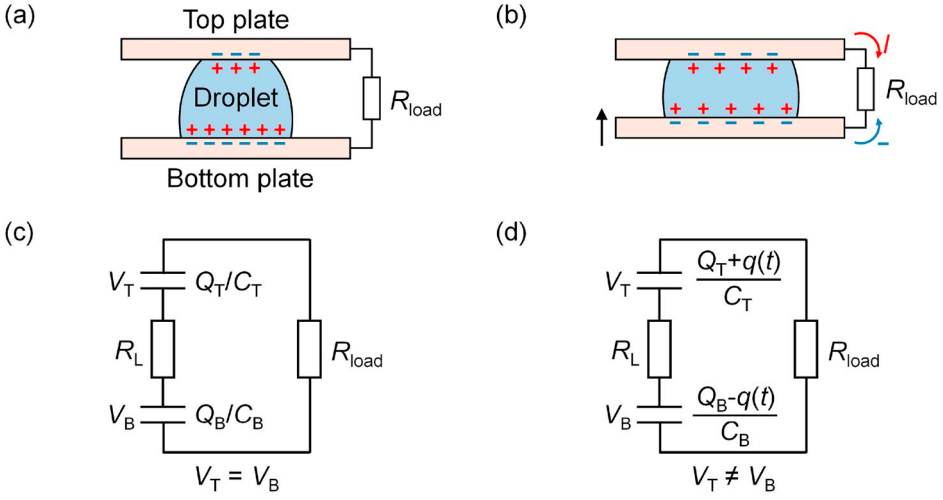

Fig. 3. Schematic of the working principle and the equivalent electrical circuits of the vibrational droplet TENG. (a) Initially, the system is in equilibrium. (b) During vibration, the electrons flow through the external circuit due to the variations of the contact areas between the droplet and the plates. (c) The equivalent electrical circuit for the initial state. (d) The equivalent electrical circuit during the vibration.

4. Results and discussion

4.1. Device structures

4.1.1. Experimental results

The effects of the device structures on the output performance of the single-droplet devices were studied. Fig. 1 depicts six types of structures of the vibrational droplet TENGs. For the structures V1 and V2, each contained two hydrophobic plates, while the structure V1 also included a dielectric layer. For the structures V3–V6, each contained a hydrophobic plate and a hydrophilic plate, while the structures V3–V5 involved dielectric layers at different locations. The output performance of these devices was tested with a water droplet of 40 μl, an initial gap of 2.5 mm, and a load resistor of 10 MΩ. The bottom plate was oscillated in sine waveform with a frequency of 1 Hz and an amplitude of 0.6 mm.

The output voltage and power of different device structures are shown in Fig. 4. It is found that the devices with two hydrophobic plates (V1 and V2) generated lower voltage (power) than those with one hydrophobic and one hydrophilic plates (V3–V6). When both plates are hydrophobic, it was observed that the contact areas of the droplet on both plates ($A_T(t)$ and $A_B(t)$) varied synchronously during the oscillation period. According to Eq. (3), the synchronous variations of the top and bottom contact areas resulted in a smaller potential difference between the top and bottom electrodes. In an extreme case that the top and bottom contact areas are equal to each other all over the oscillation period, charge transfer does not take place and output voltage cannot be generated. Therefore, devices where both plates are hydrophobic produced smaller output voltage (power).

For the devices that contained only one hydrophobic plate (V3–V6), it can be seen that the presence of the dielectric layer showed a significant influence on the output voltage and power. By comparing the structures V5 and V6, it is found that the output power was decreased by adding a dielectric layer to the hydrophobic plate. By comparing the structures V3 and V4, it is found that the output power was improved when a dielectric layer was added to the hydrophobic plate. Inserting a dielectric layer into the device does not always reduce the electrical output.

4.1.2. Theoretical calculations

In order to clarify the influence of the dielectric layer, theoretical calculations were performed. Here, the focus is concentrated on the devices that contain a hydrophobic plate and a hydrophilic plate (V3–V6). For the structures V3–V6, the hydrophobic and hydrophilic plates were used as the top and bottom plates, respectively, in the experiments. Therefore, Q_T and Q_B are the charges on the hydrophobic and hydrophilic surfaces, respectively. It should be noted that the surface charge Q_T intrinsically originates from the triboelectrification between the hydrophobic layer and the droplet, while the surface charge Q_B is formed due to the induction of Q_T. For clarity, Q_T and Q_B are called triboelectric charge Q_T and inductive charge Q_I, respectively. Accordingly, the hydrophobic top (C_T) and hydrophilic bottom (C_B) plates can be called triboelectric (C_T) and inductive (C_I) plates, respectively. According to the theoretical model, the dielectric layer influences the capacitances (C_T, C_I) and the surface charges (Q_T, Q_I). However, it is noted the inductive charge (Q_I) is just a function of the triboelectric charge (Q_T) and the capacitances (C_T, C_I). Hence, it is pivotal to investigate the effects of the dielectric layer on the triboelectric charge and the capacitances.

The impact on the triboelectric charge was studied via calculations. Eq. (3) and the parameters in Table S1 were used to calculate the triboelectric charge Q_T by fitting the output voltage and power in Fig. 4. Table 1 shows different structures and the corresponding triboelectric charges. By comparing the structures V3 with V4, and V5 with V6, it is found that the triboelectric charge Q_T decreased after adding a dielectric layer to the triboelectric plate. The charge reduction can be attributed to the increased distance between the triboelectric surface and the electrode, which has been proved by Yatsuzuka et al. [59,60] and Tang et al. [61]. By comparing the structures V3 with V5, and V4 with V6, it is found that the triboelectric charge Q_T was barely affected after inserting a dielectric layer to the inductive plate. As for the impact on the

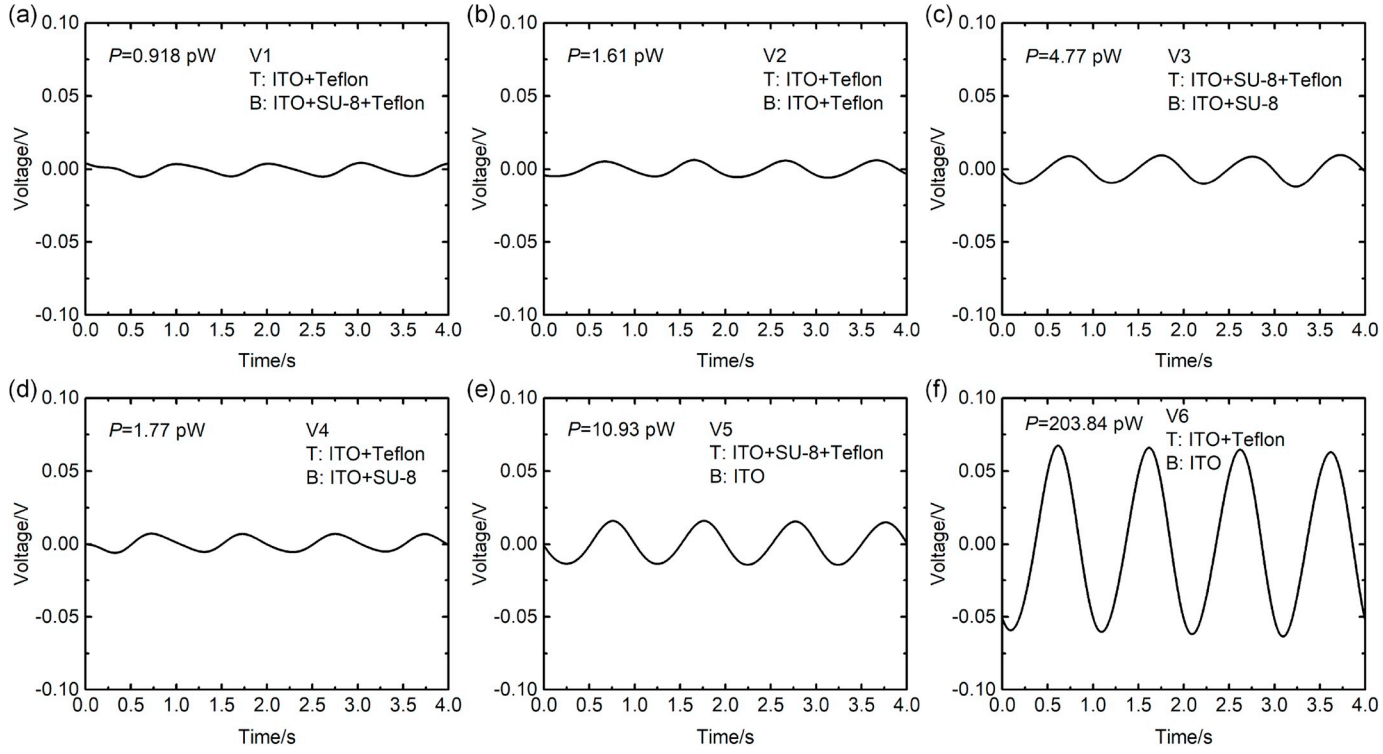

Fig. 4. Output voltage and power of different device structures. (a) Structure V1. (b) Structure V2. (c) Structure V3. (d) Structure V4. (e) Structure V5. (f) Structure V6.

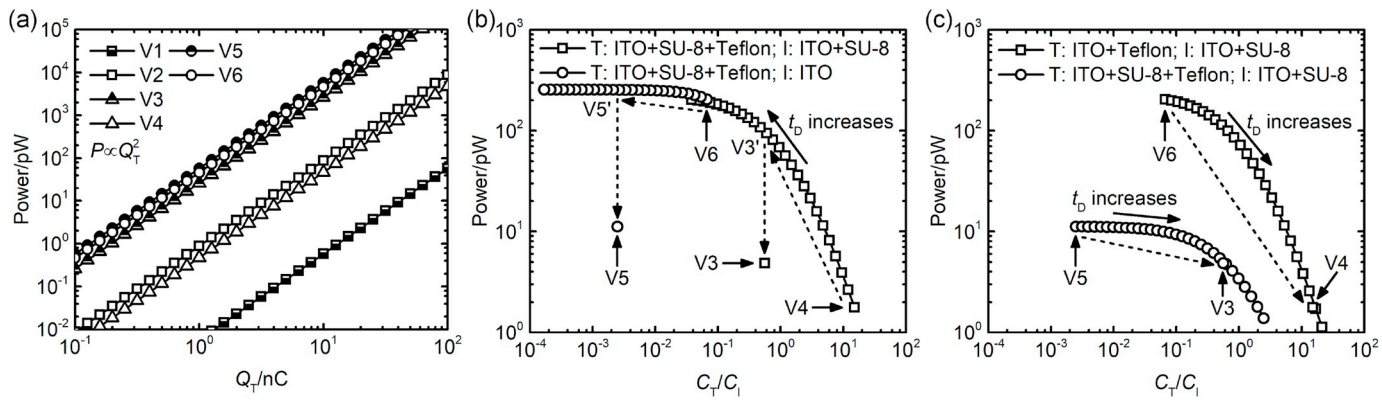

Fig. 5. Calculation results of the output power of different device structures. (a) Output power as a function of triboelectric charge. (b) Output power variation when the thickness of the dielectric layer on the triboelectric plate was varied. (c) Output power variation when the thickness of the dielectric layer on the inductive plate was varied.

Table 1
Calculation results of single-droplet devices with different structures. Power is calculated on the triboelectric charge.

Structures	Top plate	Q_T (nC)	Bottom plate	Q_B (nC)	Power (pW)
V1	ITO+Teflon	12.56	ITO+SU-8 +Teflon	0.53	0.92
V2	ITO+Teflon	1.35	ITO+Teflon	1.54	1.61
V3	ITO+SU-8 +Teflon	0.43	ITO+SU-8	0.77	4.85
V4	ITO+Teflon	1.94	ITO+SU-8	0.13	1.77
V5	ITO+SU-8 +Teflon	0.44	ITO	177.20	11.16
V6	ITO+Teflon	2.10	ITO	31.32	204.44

capacitances, it is obvious that adding a dielectric layer to the triboelectric (inductive) plate reduces the triboelectric (inductive) capacitance C_T (C_I).

After studying the variations of the triboelectric charge and the capacitances, their effects on the output power were calculated. It is found that the output power increases linearly with the square of the triboelectric charge, as shown in Fig. 5a. As for the capacitances, it is discovered that the output power increases as the tribo/inductive capacitance ratio C_T/C_I decreases, as depicted in Fig. 5b and c. The output power increases with a decreasing C_T/C_I until C_T/C_I is reduced to 0.1. When C_T/C_I is smaller than 0.1, the output power is almost not affected by C_T/C_I. It should be noted that the triboelectric capacitance C_T used here is the average capacitance over the vibration period T and is presented by

$$C_T = \frac{1}{T}\int_0^T C_T(t)\mathrm{d}t \tag{4}$$

From the above discussion, adding a dielectric layer to the triboelectric plate reduces both the triboelectric charge Q_T and the tribo/inductive capacitance ratio C_T/C_I. Since the reduced triboelectric charge and capacitance ratio impose opposite effects on the output power, the output power variation is determined by the more prominent factor. For a device whose capacitance ratio is smaller than 0.1, the output power is decreased after inserting a dielectric layer to the triboelectric plate, because the negative effect of the reduced triboelectric charge is more prominent. For example, when the device V6 ($C_T/C_I = 0.067$) is transformed to V5 by inserting a dielectric layer to the triboelectric plate, the output power is decreased from V6 to V5 in Fig. 5b. For a device whose capacitance ratio is larger than 10, the output power is improved when adding a dielectric layer to the triboelectric plate, because the positive impact of the reduced capacitance ratio is dominant. For instance, when the device V4 ($C_T/C_I = 15.11$) is transformed to V3 by adding a dielectric layer to the triboelectric plate, the output power is increased from V4 to V3 in Fig. 5b.

Inserting a dielectric layer to the inductive plate increases the tribo/inductive capacitance ratio C_T/C_I but barely changes the triboelectric charge Q_T. As a result, the output power is always reduced after adding a dielectric layer to the inductive plate. For example, when the device V5 (V6) is transformed to V3 (V4) by adding a dielectric layer to the inductive plate, the output power is decreased from V5 (V6) to V3 (V4), as shown in Fig. 5c.

From the above discussion, the optimum structure for maximizing the output power can be theoretically determined as follows. Since inserting a dielectric layer to the inductive plate always decreases the output power, an inductive plate without a dielectric layer (ITO) is favorable. When such inductive plate (ITO) is assembled with a triboelectric plate without a dielectric layer (ITO + Teflon), the capacitance ratio C_T/C_I is 0.067, indicating that inserting a dielectric layer to the triboelectric plate reduces the output power. Therefore, a triboelectric plate without a dielectric layer (ITO + Teflon) should be used with an inductive plate without a dielectric layer (ITO), which is just the structure V6. The experimental results shown in Fig. 4 and Fig. S2 also confirm that the structure V6 generated maximum output power.

4.2. Optimal load resistance

4.2.1. Experimental results

Fig. 6a displays the output power of the parallel-droplet devices with different droplet numbers as a function of the load resistance. The electrical output was measured with each droplet of 5 μl and an initial gap of 1.05 mm. The bottom plate was oscillated in a sine waveform with a frequency of 30 Hz and an amplitude of 0.4 mm. It was observed that the output power was enhanced from 0.04 μW to 7.55 μW as the droplet number N was increased from 1 to 70. Besides, the output power first increased and then decreased when the load resistance kept increasing. There existed an optimal load resistance that maximized the output power. Using the method described in the Supporting Information, the optimal load resistance was estimated for different droplet numbers, as shown in Fig. 6b. The optimal load resistance decreased as the droplet number increased.

Fig. 6c depicts the output power of the parallel-droplet device with different vibration frequency as a function of the load resistance. The output performance was tested with 42 × 5 μl droplets and an initial gap of 1.05 mm. The bottom plate was oscillated in a sine waveform with an amplitude of 0.4 mm. The output power also first increased and then decreased as the load resistance increased. It is shown in Fig. 6d that the optimal load resistance reduced when the vibration frequency increased.

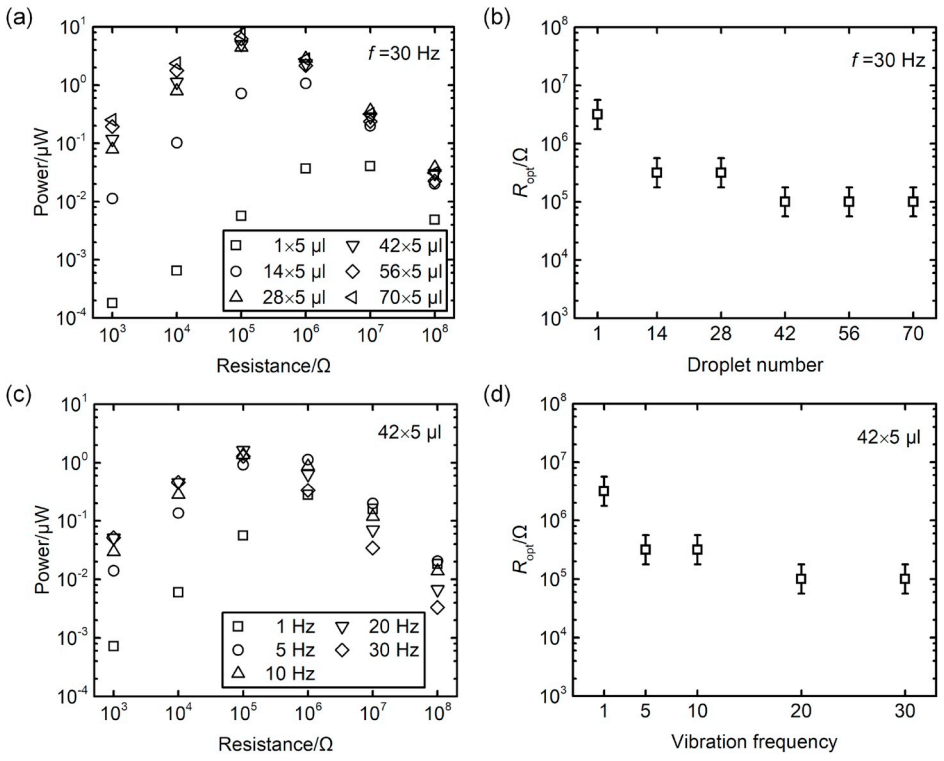

Fig. 6. Output power and optimal load resistance of the parallel-droplet devices. (a) Output power of the devices with different droplet numbers. (b) Estimated optimal load resistance as a function of droplet number. (c) Output power of the device subjected to different vibration frequencies. (d) Estimated optimal load resistance as a function of vibration frequency.

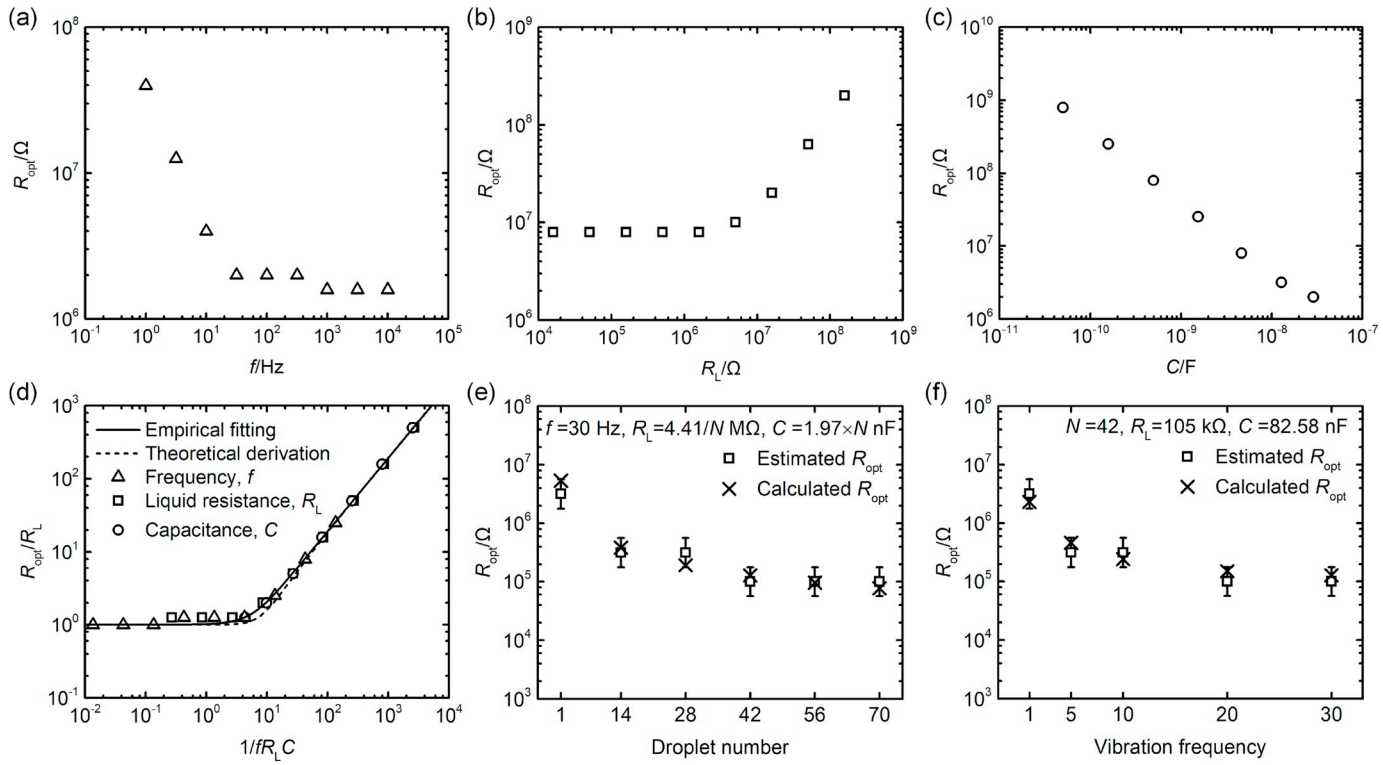

Fig. 7. Calculation results of the optimal load resistance. (a) Optimal load resistance as a function of vibration frequency. (b) Optimal load resistance as a function of droplet resistance. (c) Optimal load resistance as a function of system capacitance. (d) Empirical fitting and theoretical derivation of the optimal load resistance. (e) Estimated and calculated optimal load resistance as a function of droplet number. (f) Estimated and calculated optimal load resistance as a function of vibration frequency.

4.2.2. Empirical fitting and theoretical calculations

Eq. (3) and the parameters in Table S2 were used to calculate the optimal load resistance R_{opt} as a function of the vibration frequency f, droplet resistance R_L, and system capacitance C. The system capacitance is the average capacitance over the oscillation period T and is presented by

$$C = \frac{1}{T}\int_0^T \left(\frac{1}{C_B} + \frac{1}{C_T(t)}\right)^{-1} dt \quad (5)$$

The dependences of the optimal load resistance on the vibration frequency, droplet resistance, and system capacitance are depicted in Fig. 7a–c, respectively. It can be seen that the optimal load resistance is positively correlated with the droplet resistance and negatively correlated with the vibration frequency and system capacitance. The calculation results in Fig. 7a–c are replotted in Fig. 7d, depicting the dimensionless optimal load resistance R_{opt}/R_L as a function of the dimensionless parameter $1/fR_LC$. It can be seen that all data collapse onto a curve presented by

$$\frac{R_{opt}}{R_L} = \frac{0.191}{fR_LC} + \exp\left(-\frac{0.191}{fR_LC}\right) \quad (6)$$

This equation is the empirical formula of the optimal load resistance, by which one can calculate the optimal load resistance when the vibration frequency, droplet resistance, and system capacitance are given.

When the vibration frequency, the droplet resistance, or the system capacitance is relatively small that $1/fR_LC$ is larger than 10, the impedance of the system capacitance $1/2\pi fC$ is much larger than the droplet resistance R_L that $1/2\pi fC$ is predominant. In this case, Eq. (6) can be approximated by

$$R_{opt} = \frac{0.191}{fC} \quad (7)$$

When the vibration frequency, the droplet resistance, or the system capacitance is rather large that $1/fR_LC$ is smaller than 1, the droplet resistance R_L is much larger than the impedance of the system capacitance $1/2\pi fC$ that R_L dominates. Under this condition, Eq. (6) can be simplified as

$$R_{opt} = R_L \exp\left(-\frac{0.191}{fR_LC}\right) \approx R_L \quad (8)$$

Eq. (7) indicates that the optimal load resistance is inversely proportional to the vibration frequency when the vibration frequency is small. Similar trends have been reported for other TENGs [62,63]. Eq. (8) shows that the optimal load resistance is independent of the vibration frequency when the vibration frequency is large. The analytical results of Eqs. (7) and (8) are in good agreement with the calculation results in Fig. 7a. The dependence of the optimal load resistance on the system capacitance is the same as that on the vibration frequency. Eq. (7) shows that the optimal load resistance is independent of the droplet resistance when the droplet resistance is small. When the droplet resistance is large, Eq. (8) shows that the optimal load resistance is equal to the droplet resistance.

Alternatively, the optimal load resistance can also be derived using the Helmholtz-Thévenin theorem [64] (see Supporting Information for details). The optimal load resistances obtained from empirical curve fitting and theoretical derivation are close to each other, as shown in Fig. 7d, confirming the validity of the proposed formula.

Given the parameters in Table S2, the optimal load resistances for different working conditions were theoretically calculated using Eq. (6). The calculated results and the estimated results are plotted in Fig. 7e and f. The calculated results are in good accordance to the estimated results obtained from experiments, supporting the validity of the empirical formula. At present the optimal load resistance is determined practically by experiments with varying load resistance, which is tedious. With the empirical formula and theoretical equations, the optimal load resistance can be estimated easily and rapidly, which is of great importance to the performance improvement of the TENGs.

4.3. Serial-droplet vibrational TENG

4.3.1. Output power

The output performance of the serial-droplet vibrational TENG was tested and compared with the single-droplet and parallel-droplet devices. The serial-droplet device was tested with 80 × 5 μl droplets and an initial gap of 1.05 mm. The bottom plate was oscillated in sine waveform with the frequency of 5 Hz and the amplitude of 0.4 mm. The variation of the output power with respect to the load resistance is depicted in Fig. 8a. The output power of the serial-droplet device reached maximum 122.99 nW at load resistance 100 MΩ. For the single-droplet device, the maximum output power 40.40 nW was obtained between 1 MΩ and 10 MΩ. As for the parallel-droplet device with 70 × 5 μl droplets, the maximum output power 7.55 μW was achieved at about 0.1 MΩ. The optimal load resistance of the serial-droplet was the largest, the single-droplet was smaller, and the parallel-droplet was the smallest. This can be attributed to the droplet resistances of different devices. The total droplet resistance of the serial-droplet ($N{\cdot}R_L$) was the largest, followed by the single-droplet (R_L) and then the parallel-droplet (R_L/N). Since the optimal load resistance is positively correlated with the total droplet resistance, the optimal load resistance of these devices follow the same order of their total droplet resistances.

The variation of the power density with respect to the load resistance is shown in Fig. 8b. It can be seen that the maximum power density produced by the parallel-droplet (1.45 μW cm^{-2}) was the largest, followed by the single-droplet (0.54 μW cm^{-2}) and then the serial-droplet (20.64 nW cm^{-2}). However, according to Eq. (3), their maximum power densities should be theoretically the same, because the working condition of each droplet in these devices is identical. The discrepancy between the experimental results and the theoretical analysis was supposed to originate from the parasitic capacitance. The parasitic capacitance C_{Par} was connected in parallel with the TENG and the load, as shown in Fig. S4. For the single-droplet device, since the system capacitance was quite small, the parasitic capacitance exhibited a strong impact, decreasing the output power [65,66]. For the parallel-droplet device, its system capacitance was about N times larger than that of the single-droplet device. The system capacitance was large enough that the negative effect of the parasitic capacitance was diminished. As for the serial-droplet device, its system capacitance was about N times smaller than that of the single-droplet device. Therefore, the parasitic capacitance gave rise to a more dramatic reduction in output power.

4.3.2. Output voltage

The variation of the output voltage with respect to the load resistance is displayed in Fig. 8c. The output voltage increased and then plateaued as the load resistance increased. The maximum output voltage of the serial-droplet, parallel-droplet, and single-droplet devices were 4.33 V, 1.78 V, and 0.70 V, respectively. Given that the load resistance is infinitely large, the equivalent electrical circuit is depicted in Fig. 8d. When the triboelectric capacitance C_T is maximized (minimized), the maximum voltage V_{max} (minimum voltage V_{min}) is achieved. The maximum output voltage should be V_{max}-V_{min}. Therefore, the theoretical values of the maximum output voltage of the single-droplet, parallel-droplet, and serial-droplet devices are respectively presented by

$$V_{Single,theo} = \frac{Q_T}{C_{T,min}} - \frac{Q_T}{C_{T,max}} \quad (9)$$

$$V_{Parallel,theo} = \frac{NQ_T}{NC_{T,min}} - \frac{NQ_T}{NC_{T,max}} = \frac{Q_T}{C_{T,min}} - \frac{Q_T}{C_{T,max}} \quad (10)$$

$$V_{Serial,theo} = \frac{Q_T}{\frac{C_{T,min}}{N}} - \frac{Q_T}{\frac{C_{T,max}}{N}} = N\left(\frac{Q_T}{C_{T,min}} - \frac{Q_T}{C_{T,max}}\right) \quad (11)$$

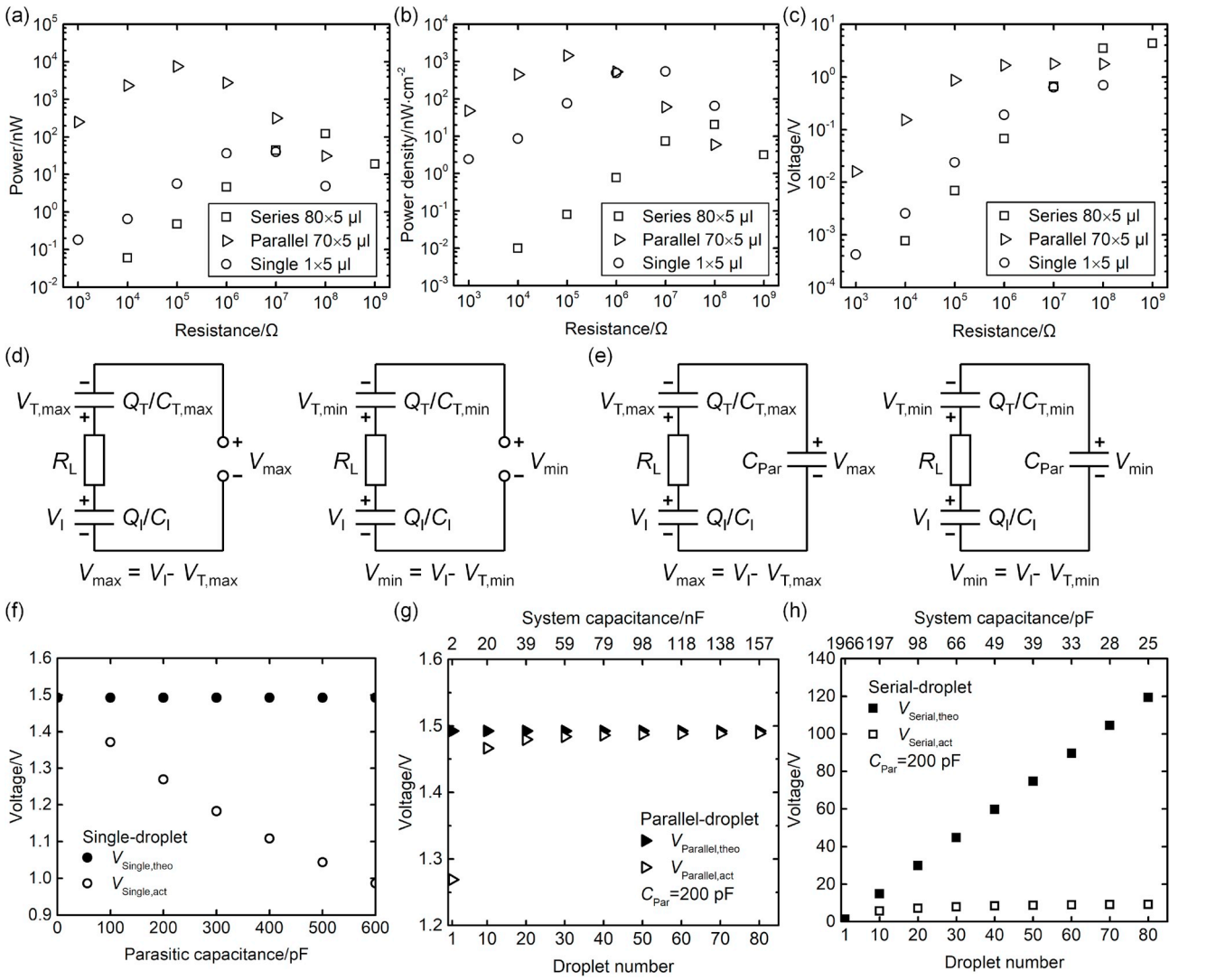

Fig. 8. Output performance of the serial-droplet, parallel-droplet, and single-droplet devices. (a) Output power as a function of load resistance. (b) Power density as a function of load resistance. (c) Output voltage as a function of load resistance. (d) Equivalent electrical circuit of the maximum output voltage when parasitic capacitance is not considered. (e) Equivalent electrical circuit of the maximum output voltage when parasitic capacitance is considered. (f) The theoretical and actual maximum output voltage of the single-droplet device as a function of parasitic capacitance. (g) The theoretical and actual maximum output voltage of the parallel-droplet device as a function of droplet number. (h) The theoretical and actual maximum output voltage of the serial-droplet device as a function of droplet number.

where $C_{T,max}$ and $C_{T,min}$ are the maximum and minimum values of the triboelectric capacitance, respectively, and N is the droplet number. According to Eq. (9)-(11), $V_{Parallel}$ should be equal to V_{Single}, while V_{Serial} should be N times of V_{Single}. In the present experiments, however, the parallel-droplet generated much larger output voltage than the single-droplet. The serial-droplet device, which contained 80 droplets arranged in series, produced only 6-fold output voltage compared with the single-droplet. The discrepancy between the experimental results and the theoretical derivation was probably caused by the parasitic capacitance. Since the system capacitance of the TENG is quite small, it is important to take the parasitic capacitance into account [65,66]. When the parasitic capacitance is included in the equivalent electrical circuit, as shown in Fig. 8e, the actual values of the maximum output voltage are expressed as

$$V_{Single,act} = \frac{1}{1+\frac{C_{Par}}{C_I}+\frac{C_{Par}}{C_{T,max}}}\left(\frac{Q_I}{C_I}-\frac{Q_T}{C_{T,max}}\right)+\frac{1}{1+\frac{C_{Par}}{C_I}+\frac{C_{Par}}{C_{T,min}}}\left(\frac{Q_T}{C_{T,min}}-\frac{Q_I}{C_I}\right) \quad (12)$$

$$V_{Parallel,act} = \frac{1}{1+\frac{C_{Par}}{NC_I}+\frac{C_{Par}}{NC_{T,max}}}\left(\frac{NQ_I}{NC_I}-\frac{NQ_T}{NC_{T,max}}\right) + \frac{1}{1+\frac{C_{Par}}{NC_I}+\frac{C_{Par}}{NC_{T,min}}}\left(\frac{NQ_T}{NC_{T,min}}-\frac{NQ_I}{NC_I}\right) = \frac{1}{1+\frac{C_{Par}}{NC_I}+\frac{C_{Par}}{NC_{T,max}}}\left(\frac{Q_I}{C_I}-\frac{Q_T}{C_{T,max}}\right)+\frac{1}{1+\frac{C_{Par}}{NC_I}+\frac{C_{Par}}{NC_{T,min}}}\left(\frac{Q_T}{C_{T,min}}-\frac{Q_I}{C_I}\right) \quad (13)$$

$$V_{\text{Serial,act}} = \frac{1}{1+\frac{NC_{\text{Par}}}{C_{\text{I}}}+\frac{NC_{\text{Par}}}{C_{\text{T,max}}}}\left(\frac{Q_{\text{I}}}{\frac{C_{\text{I}}}{N}}-\frac{Q_{\text{T}}}{\frac{C_{\text{T,max}}}{N}}\right) + \frac{1}{1+\frac{NC_{\text{Par}}}{C_{\text{I}}}+\frac{NC_{\text{Par}}}{C_{\text{T,min}}}}\left(\frac{Q_{\text{T}}}{\frac{C_{\text{T,min}}}{N}}-\frac{Q_{\text{I}}}{\frac{C_{\text{I}}}{N}}\right) = \frac{1}{\frac{1}{N}+\frac{C_{\text{Par}}}{C_{\text{I}}}+\frac{C_{\text{Par}}}{C_{\text{T,max}}}}\left(\frac{Q_{\text{I}}}{C_{\text{I}}}-\frac{Q_{\text{T}}}{C_{\text{T,max}}}\right) + \frac{1}{\frac{1}{N}+\frac{C_{\text{Par}}}{C_{\text{I}}}+\frac{C_{\text{Par}}}{C_{\text{T,min}}}}\left(\frac{Q_{\text{T}}}{C_{\text{T,min}}}-\frac{Q_{\text{I}}}{C_{\text{I}}}\right) \quad (14)$$

Eq. (9) and Eq. (12) are plotted in Fig. 8f. It can be seen that the actual voltage of the single-droplet decreases as the parasitic capacitance increases. By comparing Eq. (13) with Eq. (12), it is noted that the parallel connection of the droplets increases the system capacitance ($N{\cdot}C_{\text{I}}$ and $N{\cdot}C_{\text{T}}$), which diminishes the impact of the parasitic capacitance and thereby increases the actual voltage, as shown in Fig. 8g. By comparing Eq. (14) with Eq. (12), it can be found that the serial connection of the droplets decreases the system capacitance to C_{I}/N and C_{T}/N, which increases the negative impact of the parasitic capacitance. Therefore, the deviation of the actual voltage from the theoretical value increases with the increasing droplet number, as shown in Fig. 8h. Although the serial-droplet still generates higher voltage than the single-droplet, the output voltage enhancement obtained is not as remarkable as expected.

Besides the parasitic capacitance, the triboelectric charge density is also an important factor for the output discrepancy. The triboelectric charge density is dominant in determining the output. However, it is difficult to obtain the accurate value of the triboelectric charge density from experiment. The triboelectric charge used in calculation is only an estimated value, which inevitably leads to discrepancy.

For the multiple droplet devices, the desynchronization effect is another important factor for the output discrepancy. The contact area $A_{\text{T}}(t)$ of each droplet cannot perfectly synchronize with each other during oscillation, because all droplets are not exactly the same size, the hydrophobic coating is not absolutely uniform, and the top and bottom plates are not absolutely parallel. Since the desynchronization effect varies from case to case, it is hard to involve it in the calculations.

5. Conclusions

Vibrational droplet TENGs with different structures were experimentally studied and theoretically analyzed. When the tribo/inductive capacitance ratio was larger than 10, adding a dielectric layer to the triboelectric plate increased the output power. When the tribo/inductive capacitance ratio was smaller than 0.1, inserting a dielectric layer to the triboelectric plate decreased the output power. Addition of a dielectric layer to the inductive plate always diminished the output power. The dependence of the optimal load resistance was also investigated. The optimal load resistance was positively correlated with the droplet resistance and negatively correlated with the vibration frequency and the system capacitance. Empirical formula and theoretical equations were developed for calculating the optimal load resistance. The output performance of the serial-droplet device was tested. Compared to the single-droplet and parallel-droplet devices, the serial-droplet device generated the lowest power density but produced the largest output voltage. Since the system capacitance of the serial-droplet device was very small, its output performance was drastically impaired by the parasitic capacitance, leading to a much smaller output power and voltage enhancement.

Declaration of competing interests

The authors declare that they have no known competing financial interests or personal relationships that could have appeared to influence the work reported in this paper.

Acknowledgement

This work is supported by the Joint Research Fund for Overseas Chinese Scholars and Scholars in Hong Kong and Macao, China(Grant No. 51728602) and Science Fund for Creative Research Groups of the National Natural Science Foundation of China, China (Grant No. 51721004).

Appendix A. Supplementary data

Supplementary data to this article can be found online at https://doi.org/10.1016/j.nanoen.2020.104473.

References

[1] Z.L. Wang, Triboelectric nanogenerators as new energy technology and self-powered sensors - principles, problems and perspectives, Faraday Discuss 176 (2014) 447–458, https://doi.org/10.1039/c4fd00159a.
[2] X. Cao, Y. Jie, N. Wang, Z.L. Wang, Triboelectric nanogenerators driven self-powered electrochemical processes for energy and environmental science, Adv. Energy Mater. 6 (2016), 1600665, https://doi.org/10.1002/aenm.201600665.
[3] Z.L. Wang, On maxwell's displacement current for energy and sensors: the origin of nanogenerators, Mater. Today 20 (2017) 74–82, https://doi.org/10.1016/j.mattod.2016.12.001.
[4] G. Zhu, Z.H. Lin, Q. Jing, P. Bai, C. Pan, Y. Yang, Y. Zhou, Z.L. Wang, Toward large-scale energy harvesting by a nanoparticle-enhanced triboelectric nanogenerator, Nano Lett. 13 (2013) 847–853, https://doi.org/10.1021/nl4001053.
[5] J. Chen, G. Zhu, W. Yang, Q. Jing, P. Bai, Y. Yang, T.C. Hou, Z.L. Wang, Harmonic-resonator-based triboelectric nanogenerator as a sustainable power source and a self-powered active vibration sensor, Adv. Mater. 25 (2013) 6094–6099, https://doi.org/10.1002/adma.201302397.
[6] F.-R. Fan, Z.-Q. Tian, Z.L. Wang, Flexible triboelectric generator, Nano Energy 1 (2012) 328–334, https://doi.org/10.1016/j.nanoen.2012.01.004.
[7] X.S. Zhang, M.D. Han, R.X. Wang, F.Y. Zhu, Z.H. Li, W. Wang, H.X. Zhang, Frequency-multiplication high-output triboelectric nanogenerator for sustainably powering biomedical microsystems, Nano Lett. 13 (2013) 1168–1172, https://doi.org/10.1021/nl3045684.
[8] P. Bai, G. Zhu, Z.H. Lin, Q. Jing, J. Chen, G. Zhang, J. Ma, Z.L. Wang, Integrated multilayered triboelectric nanogenerator for harvesting biomechanical energy from human motions, ACS Nano 7 (2013) 3713–3719, https://doi.org/10.1021/nn4007708.
[9] G. Zhu, P. Bai, J. Chen, Z.L. Wang, Power-generating shoe insole based on triboelectric nanogenerators for self-powered consumer electronics, Nano Energy 2 (2013) 688–692, https://doi.org/10.1016/j.nanoen.2013.08.002.
[10] L. Lin, S. Wang, Y. Xie, Q. Jing, S. Niu, Y. Hu, Z.L. Wang, Segmentally structured disk triboelectric nanogenerator for harvesting rotational mechanical energy, Nano Lett. 13 (2013) 2916–2923, https://doi.org/10.1021/nl4013002.
[11] G. Zhu, J. Chen, T. Zhang, Q. Jing, Z.L. Wang, Radial-arrayed rotary electrification for high performance triboelectric generator, Nat. Commun. 5 (2014) 3426, https://doi.org/10.1038/ncomms4426.
[12] C. Zhang, T. Zhou, W. Tang, C. Han, L. Zhang, Z.L. Wang, Rotating-disk-based direct-current triboelectric nanogenerator, Adv. Energy Mater. 4 (2014), 1301798, https://doi.org/10.1002/aenm.201301798.
[13] W. Du, X. Han, L. Lin, M. Chen, X. Li, C. Pan, Z.L. Wang, A three dimensional multi-layered sliding triboelectric nanogenerator, Adv. Energy Mater. 4 (2014), 1301592, https://doi.org/10.1002/aenm.201301592.
[14] G. Cheng, L. Zheng, Z.-H. Lin, J. Yang, Z. Du, Z.L. Wang, Multilayered-electrode-based triboelectric nanogenerators with managed output voltage and multifold enhanced charge transport, Adv. Energy Mater. 5 (2015), 1401452, https://doi.org/10.1002/aenm.201401452.
[15] Y. Xie, S. Wang, S. Niu, L. Lin, Q. Jing, Y. Su, Z. Wu, Z.L. Wang, Multi-layered disk triboelectric nanogenerator for harvesting hydropower, Nano Energy 6 (2014) 129–136, https://doi.org/10.1016/j.nanoen.2014.03.015.
[16] S. Wang, Y. Xie, S. Niu, L. Lin, Z.L. Wang, Freestanding triboelectric-layer-based nanogenerators for harvesting energy from a moving object or human motion in contact and non-contact modes, Adv. Mater. 26 (2014) 2818–2824, https://doi.org/10.1002/adma.201305303.
[17] T.C. Hou, Y. Yang, H. Zhang, J. Chen, L.J. Chen, Z.L. Wang, Triboelectric nanogenerator built inside shoe insole for harvesting walking energy, Nano Energy 2 (2013) 856–862, https://doi.org/10.1016/j.nanoen.2013.03.001.
[18] W. Yang, J. Chen, G. Zhu, J. Yang, P. Bai, Y. Su, Q. Jing, X. Cao, Z.L. Wang, Harvesting energy from the natural vibration of human walking, ACS Nano 7 (2013) 11317–11324, https://doi.org/10.1021/nn405175z.
[19] J. Zhong, Q. Zhong, F. Fan, Y. Zhang, S. Wang, B. Hu, Z.L. Wang, J. Zhou, Finger typing driven triboelectric nanogenerator and its use for instantaneously lighting up leds, Nano Energy 2 (2013) 491–497, https://doi.org/10.1016/j.nanoen.2012.11.015.

[20] W. Yang, J. Chen, Q. Jing, J. Yang, X. Wen, Y. Su, G. Zhu, P. Bai, Z.L. Wang, 3d stack integrated triboelectric nanogenerator for harvesting vibration energy, Adv. Funct. Mater. 24 (2014) 4090–4096, https://doi.org/10.1002/adfm.201304211.
[21] Y. Xie, S. Wang, L. Lin, Q. Jing, Z.H. Lin, S. Niu, Z. Wu, Z.L. Wang, Rotary triboelectric nanogenerator based on a hybridized mechanism for harvesting wind energy, ACS Nano 7 (2013) 7119–7125, https://doi.org/10.1021/nn402477h.
[22] Y. Yang, G. Zhu, H. Zhang, J. Chen, X. Zhong, Z.H. Lin, Y. Su, P. Bai, X. Wen, Z. L. Wang, Triboelectric nanogenerator for harvesting wind energy and as self-powered wind vector sensor system, ACS Nano 7 (2013) 9461–9468, https://doi.org/10.1021/nn4043157.
[23] J. Bae, J. Lee, S. Kim, J. Ha, B.S. Lee, Y. Park, C. Choong, J.B. Kim, Z.L. Wang, H. Y. Kim, J.J. Park, U.I. Chung, Flutter-driven triboelectrification for harvesting wind energy, Nat. Commun. 5 (2014) 4929, https://doi.org/10.1038/ncomms5929.
[24] Y. Hu, J. Yang, Q. Jing, S. Niu, W. Wu, Z.L. Wang, Triboelectric nanogenerator built on suspended 3d spiral structure as vibration and positioning sensor and wave energy harvester, ACS Nano 7 (2013) 10424–10432, https://doi.org/10.1021/nn405209u.
[25] Y. Yang, H. Zhang, R. Liu, X. Wen, T.-C. Hou, Z.L. Wang, Fully enclosed triboelectric nanogenerators for applications in water and harsh environments, Adv. Energy Mater. 3 (2013) 1563–1568, https://doi.org/10.1002/aenm.201300376.
[26] X.F. Wang, S.M. Niu, Y.J. Yin, F. Yi, Z. You, Z.L. Wang, Triboelectric nanogenerator based on fully enclosed rolling spherical structure for harvesting low-frequency water wave energy, Adv. Energy Mater. 5 (2015), 1501467, https://doi.org/10.1002/aenm.201501467.
[27] P. Bai, G. Zhu, Q. Jing, J. Yang, J. Chen, Y. Su, J. Ma, G. Zhang, Z.L. Wang, Membrane-based self-powered triboelectric sensors for pressure change detection and its uses in security surveillance and healthcare monitoring, Adv. Funct. Mater. 24 (2014) 5807–5813, https://doi.org/10.1002/adfm.201401267.
[28] B.C. Han, C. Zhang, X.H. Li, L. Zhang, T. Zhou, W. Hu, Z.L. Wang, Self-powered velocity and trajectory tracking sensor array made of planar triboelectric nanogenerator pixels, Nano Energy 9 (2014) 325–333, https://doi.org/10.1016/j.nanoen.2014.07.025.
[29] F. Yi, L. Lin, S. Niu, J. Yang, W. Wu, S. Wang, Q. Liao, Y. Zhang, Z.L. Wang, Self-powered trajectory, velocity, and acceleration tracking of a moving object/body using a triboelectric sensor, Adv. Funct. Mater. 24 (2014) 7488–7494, https://doi.org/10.1002/adfm.201402703.
[30] H. Zhang, Y. Yang, Y. Su, J. Chen, K. Adams, S. Lee, C. Hu, Z.L. Wang, Triboelectric nanogenerator for harvesting vibration energy in full space and as self-powered acceleration sensor, Adv. Funct. Mater. 24 (2014) 1401–1407, https://doi.org/10.1002/adfm.201302453.
[31] H. Guo, Q. Leng, X. He, M. Wang, J. Chen, C. Hu, Y. Xi, A triboelectric generator based on checker-like interdigital electrodes with a sandwiched pet thin film for harvesting sliding energy in all directions, Adv. Energy Mater. 5 (2015), 1400790, https://doi.org/10.1002/aenm.201400790.
[32] Y. Jie, N. Wang, X. Cao, Y. Xu, T. Li, X. Zhang, Z.L. Wang, Self-powered triboelectric nanosensor with poly(tetrafluoroethylene) nanoparticle arrays for dopamine detection, ACS Nano 9 (2015) 8376–8383, https://doi.org/10.1021/acsnano.5b03052.
[33] Z. Li, J. Chen, H. Guo, X. Fan, Z. Wen, M.-H. Yeh, C. Yu, X. Cao, Z.L. Wang, Triboelectrification-enabled self-powered detection and removal of heavy metal ions in wastewater, Adv. Mater. 28 (2016) 2983–2991, https://doi.org/10.1002/adma.201504356.
[34] Q. Jiang, Y. Han, W. Tang, H. Zhu, C. Gao, S. Chen, M. Willander, X. Cao, Z. L. Wang, Self-powered seawater desalination and electrolysis using flowing kinetic energy, Nano Energy 15 (2015) 266–274, https://doi.org/10.1016/j.nanoen.2015.04.036.
[35] S. Chen, C. Gao, W. Tang, H. Zhu, Y. Han, Q. Jiang, T. Li, X. Cao, Z. Wang, Self-powered cleaning of air pollution by wind driven triboelectric nanogenerator, Nano Energy 14 (2015) 217–225, https://doi.org/10.1016/j.nanoen.2014.12.013.
[36] G. Zhu, C. Pan, W. Guo, C.Y. Chen, Y. Zhou, R. Yu, Z.L. Wang, Triboelectric-generator-driven pulse electrodeposition for micropatterning, Nano Lett. 12 (2012) 4960–4965, https://doi.org/10.1021/nl302560k.
[37] W. Tang, Y. Han, C.B. Han, C.Z. Gao, X. Cao, Z.L. Wang, Self-powered water splitting using flowing kinetic energy, Adv. Mater. 27 (2015) 272–276, https://doi.org/10.1002/adma.201404071.
[38] C. Bao Han, W. Du, C. Zhang, W. Tang, L. Zhang, Z.L. Wang, Harvesting energy from automobile brake in contact and non-contact mode by conjunction of triboelectrication and electrostatic-induction processes, Nano Energy 6 (2014) 59–65, https://doi.org/10.1016/j.nanoen.2014.03.009.
[39] Y. Xie, S. Wang, S. Niu, L. Lin, Q. Jing, J. Yang, Z. Wu, Z.L. Wang, Grating-structured freestanding triboelectric-layer nanogenerator for harvesting mechanical energy at 85% total conversion efficiency, Adv. Mater. 26 (2014) 6599–6607, https://doi.org/10.1002/adma.201402428.
[40] J. Chen, J. Yang, H. Guo, Z. Li, L. Zheng, Y. Su, Z. Wen, X. Fan, Z.L. Wang, Automatic mode transition enabled robust triboelectric nanogenerators, ACS Nano 9 (2015) 12334–12343, https://doi.org/10.1021/acsnano.5b05618.
[41] S. Li, S. Wang, Y. Zi, Z. Wen, L. Lin, G. Zhang, Z.L. Wang, Largely improving the robustness and lifetime of triboelectric nanogenerators through automatic transition between contact and noncontact working states, ACS Nano 9 (2015) 7479–7487, https://doi.org/10.1021/acsnano.5b02575.
[42] L.B. Huang, G. Bai, M.C. Wong, Z. Yang, W. Xu, J. Hao, Magnetic-assisted noncontact triboelectric nanogenerator converting mechanical energy into electricity and light emissions, Adv. Mater. 28 (2016) 2744–2751, https://doi.org/10.1002/adma.201505839.
[43] L.B. Huang, W. Xu, G.X. Bai, M.C. Wong, Z.B. Yang, J.H. Hao, Wind energy and blue energy harvesting based on magnetic-assisted noncontact triboelectric nanogenerator, Nano Energy 30 (2016) 36–42, https://doi.org/10.1016/j.nanoen.2016.09.032.
[44] T. Krupenkin, J.A. Taylor, Reverse electrowetting as a new approach to high-power energy harvesting, Nat. Commun. 2 (2011) 448, https://doi.org/10.1038/ncomms1454.
[45] S.H. Kwon, J. Park, W.K. Kim, Y.J. Yang, E. Lee, C.J. Han, S.Y. Park, J. Lee, Y. S. Kim, An effective energy harvesting method from a natural water motion active transducer, Energy Environ. Sci. 7 (2014) 3279–3283, https://doi.org/10.1039/C4EE00588K.
[46] J.K. Moon, J. Jeong, D. Lee, H.K. Pak, Electrical power generation by mechanically modulating electrical double layers, Nat. Commun. 4 (2013) 1487, https://doi.org/10.1038/ncomms2485.
[47] L.E. Helseth, X.D. Guo, Contact electrification and energy harvesting using periodically contacted and squeezed water droplets, Langmuir 31 (2015) 3269–3276, https://doi.org/10.1021/la503494c.
[48] W. Kong, P. Cao, X. He, L. Yu, X. Ma, Y. He, L. Lu, X. Zhang, Y. Deng, Ionic liquid based vibrational energy harvester by periodically squeezing the liquid bridge, RSC Adv. 4 (2014) 19356–19361, https://doi.org/10.1039/c4ra00629a.
[49] Y. Su, X. Wen, G. Zhu, J. Yang, J. Chen, P. Bai, Z. Wu, Y. Jiang, Z.L. Wang, Hybrid triboelectric nanogenerator for harvesting water wave energy and as a self-powered distress signal emitter, Nano Energy 9 (2014) 186–195, https://doi.org/10.1016/j.nanoen.2014.07.006.
[50] Y. Jie, Q. Jiang, Y. Zhang, N. Wang, X. Cao, A structural bionic design: from electric organs to systematic triboelectric generators, Nano Energy 27 (2016) 554–560, https://doi.org/10.1016/j.nanoen.2016.07.028.
[51] Y. Jie, X. Jia, J. Zou, Y. Chen, N. Wang, Z.L. Wang, X. Cao, Natural leaf made triboelectric nanogenerator for harvesting environmental mechanical energy, Adv. Energy Mater. 8 (2018), 1703133, https://doi.org/10.1002/aenm.201703133.
[52] D.C. Grahame, The electrical double layer and the theory of electrocapillarity, Chem. Rev. 41 (1947) 441–501, https://doi.org/10.1021/cr60130a002.
[53] R. Parsons, The electrical double layer: recent experimental and theoretical developments, Chem. Rev. 90 (1990) 813–826, https://doi.org/10.1021/cr00103a008.
[54] R. Zimmermann, S. Dukhin, C. Werner, Electrokinetic measurements reveal interfacial charge at polymer films caused by simple electrolyte ions, J. Phys. Chem. B 105 (2001) 8544–8549, https://doi.org/10.1021/jp004051u.
[55] R.B. Schoch, J. Han, P. Renaud, Transport phenomena in nanofluidics, Rev. Mod. Phys. 80 (2008) 839–883, https://doi.org/10.1103/RevModPhys.80.839.
[56] D. Qu, H. Shi, Studies of activated carbons used in double-layer capacitors, J. Power Sources 74 (1998) 99–107, https://doi.org/10.1016/s0378-7753(98)00038-x.
[57] P. Simon, Y. Gogotsi, Materials for electrochemical capacitors, Nat. Mater. 7 (2008) 845–854, https://doi.org/10.1038/nmat2297.
[58] P. Sharma, T.S. Bhatti, A review on electrochemical double-layer capacitors, Energy Convers. Manag. 51 (2010) 2901–2912, https://doi.org/10.1016/j.enconman.2010.06.031.
[59] K. Yatsuzuka, Y. Mizuno, K. Asano, Electrification phenomena of pure water droplets dripping and sliding on a polymer surface, J. Electrost. 32 (1994) 157–171, https://doi.org/10.1016/0304-3886(94)90005-1.
[60] K. Yatsuzuka, Y. Higashiyama, K. Asano, Electrification of polymer surface caused by sliding ultrapure water, IEEE Trans. Ind. Appl. 32 (1996) 825–831, https://doi.org/10.1109/28.511638.
[61] W. Tang, T. Jiang, F.R. Fan, A.F. Yu, C. Zhang, X. Cao, Z.L. Wang, Liquid-metal electrode for high-performance triboelectric nanogenerator at an instantaneous energy conversion efficiency of 70.6%, Adv. Funct. Mater. 25 (2015) 3718–3725, https://doi.org/10.1002/adfm.201501331.
[62] S. Niu, S. Wang, L. Lin, Y. Liu, Y.S. Zhou, Y. Hu, Z.L. Wang, Theoretical study of contact-mode triboelectric nanogenerators as an effective power source, Energy Environ. Sci. 6 (2013) 3576–3583, https://doi.org/10.1039/c3ee42571a.
[63] S. Niu, Z.L. Wang, Theoretical systems of triboelectric nanogenerators, Nano Energy 14 (2015) 161–192, https://doi.org/10.1016/j.nanoen.2014.11.034.
[64] D.H. Johnson, Origins of the equivalent circuit concept: the voltage-source equivalent, Proc. IEEE 91 (2003) 636–640, https://doi.org/10.1109/jproc.2003.811716.
[65] S. Boisseau, G. Despesse, T. Ricart, E. Defay, A. Sylvestre, Cantilever-based electret energy harvesters, Smart Mater. Struct. 20 (2011) 105013, https://doi.org/10.1088/0964-1726/20/10/105013.
[66] S. Boisseau, G. Despesse, B.A. Seddik, Electrostatic conversion for vibration energy harvesting, in: M. Lallart (Ed.), Small-scale Energy Harvesting, IntechOpen, London, UK, 2012, pp. 92–134.

Jing Ding received his B.S. degree from Xi'an Jiaotong University in 2013. He is currently a Ph.D. candidate in the Key Laboratory of Thermo-Fluid Science and Engineering of MOE at Xi'an Jiaotong University. His research interests include energy harvesting and electromicrofluidics (EMF).

Wen-Quan Tao is currently a professor of Xi'an Jiaotong University. He is the Associate editor of International Journal of Heat & Mass Transfer and Computers & Fluids. He is also a member of Advisory Board of Numerical Heat Transfer and Progress in Computational Fluid Dynamics. His current research interests include PEMFC, cooling technologies of data center and applications of microfluidics.

Shih-Kang Fan received his B.S. degree from National Central University, Taiwan in 1996, M.S. and Ph.D. degrees from the University of California, Los Angeles (UCLA) in 2001 and 2003, respectively. He was a faculty member in National Chiao Tung University, Taiwan from 2004 to 2012 and then in National Taiwan University, Taiwan from 2012 to 2019. He is now a Professor in the Department of Mechanical and Nuclear Engineering at Kansas State University. Dr. Fan's research interests include electrowetting, electromicrofluidics, tissue engineering, *in vitro* diagnosis, and energy.